



HAL
open science

Solar Wind Ion Sputtering from Airless Planetary Bodies: New Insights into the Surface Binding Energies for Elements in Plagioclase Feldspars

Liam S Morrissey, Stefan Bringuier, Caixia Bu, Matthew H Burger, Chuanfei Dong, Denton S Ebel, George E Harlow, Ziyu Huang, Rosemary M Killen, François Leblanc, et al.

► To cite this version:

Liam S Morrissey, Stefan Bringuier, Caixia Bu, Matthew H Burger, Chuanfei Dong, et al.. Solar Wind Ion Sputtering from Airless Planetary Bodies: New Insights into the Surface Binding Energies for Elements in Plagioclase Feldspars. *The Planetary Science Journal*, 2024, 5 (12), pp.272. 10.3847/PSJ/ad8eaf. hal-04830827

HAL Id: hal-04830827

<https://hal.science/hal-04830827v1>

Submitted on 11 Dec 2024

HAL is a multi-disciplinary open access archive for the deposit and dissemination of scientific research documents, whether they are published or not. The documents may come from teaching and research institutions in France or abroad, or from public or private research centers.

L'archive ouverte pluridisciplinaire **HAL**, est destinée au dépôt et à la diffusion de documents scientifiques de niveau recherche, publiés ou non, émanant des établissements d'enseignement et de recherche français ou étrangers, des laboratoires publics ou privés.



Distributed under a Creative Commons Attribution 4.0 International License



Solar Wind Ion Sputtering from Airless Planetary Bodies: New Insights into the Surface Binding Energies for Elements in Plagioclase Feldspars

Liam S. Morrissey^{1,2}, Stefan Bringuier³, Caixia Bu⁴, Matthew H. Burger⁵, Chuanfei Dong⁶, Denton S. Ebel², George E. Harlow², Ziyu Huang⁶, Rosemary M. Killen⁷, Francois Leblanc⁸, Amanda Ricketts¹, Orenthal J. Tucker⁷, and

Daniel W. Savin⁴

¹ Faculty of Engineering and Applied Science, Memorial University, St. John's, NL, A1B2W4, Canada; lsm088@mun.ca

² American Museum of Natural History, New York, NY 10024, USA

³ Independent Researcher, Oceanside, CA 92056, USA

⁴ Columbia Astrophysics Laboratory, Columbia University, New York, NY 10027, USA

⁵ Space Telescope Science Institute, Baltimore, MD 21218, USA

⁶ Center for Space Physics and Department of Astronomy, Boston University, Boston, MA 02215, USA

⁷ NASA Goddard Space Flight Center, Greenbelt, MD 20771, USA

⁸ LATMOS/CNRS, Sorbonne Université, Paris, 75252, France

Received 2024 July 09; revised 2024 October 31; accepted 2024 November 01; published 2024 December 10

Abstract

Our understanding of the ion-sputtering contribution to the formation of exospheres on airless bodies has been hindered by the lack of accurate surface binding energies (SBEs) of the elements in the various mineral and amorphous compounds expected to be on the surfaces of these bodies. The SBE for a given element controls the predicted sputtering yield and energy distribution of the ejecta. Here, we use molecular dynamics computations to provide SBE data for the range of elements sputtered from plagioclase feldspar crystalline end members, albite and anorthite, which are expected to be important mineral components on the surfaces of the Moon and Mercury. Results show that the SBE is dependent on the crystal orientation and the element's coordination, meaning multiple SBEs are possible for a given element. Variation in the SBEs among the different surface positions has a significant effect on the predicted yield and energy distribution of the ejecta. We then consider sputtering by H, He, and a solar wind mixture of 96% H and 4% He. For each of these cases, we derive best-fit elemental SBE values to predict the ejecta energy distribution from each of the (001), (010), and (011) cleavage planes. We demonstrate that the He contribution to the sputtering yield cannot be accounted for by multiplying the 100% H results by some factor. Lastly, we average our results over all three possible lattice orientations and provide best-fit elemental SBE values that can be easily incorporated into sputtering yield models.

Unified Astronomy Thesaurus concepts: [Solar wind \(1534\)](#); [Mercury \(planet\) \(1024\)](#); [The Moon \(1692\)](#); [Exosphere \(499\)](#); [Space weather \(2037\)](#); [Laboratory astrophysics \(2004\)](#); [Solid matter physics \(2090\)](#); [Theoretical techniques \(2093\)](#); [Theoretical models \(2107\)](#); [Lunar surface \(974\)](#); [Planetary surfaces \(2113\)](#); [Lunar mineralogy \(962\)](#)

1. Introduction

The exospheres of the Moon and Mercury are formed, in part, by solar wind (SW) ions sputtering atoms from the surfaces of these airless bodies (J. Papike et al. 1991; W. E. McClintock et al. 2018; T. J. McCoy et al. 2018). The Moon's surface is bombarded by SW ions because it does not possess an atmosphere or intrinsic magnetic field to deflect the ions (A. R. Poppe et al. 2018; O. J. Tucker et al. 2021). Mercury is also not protected by an atmosphere, but it does possess a magnetic field of about 1% of Earth's magnetic field strength (B. J. Anderson et al. 2011; C. Dong et al. 2019). SW ions impact the surface on the dayside through the high-latitude cusps associated with the magnetic poles (J. M. Raines et al. 2022; J. Zhao et al. 2024) and on the mid-latitude nightside through magnetotail reconnection (S. Fatemi et al. 2020; A. N. Glass et al. 2022).

Our understanding of the ion-sputtering contribution to the lunar and Hermean exospheres has been hindered by a lack of

accurate surface binding energies (S. Bringuier et al. 2019; L. S. Morrissey et al. 2021; N. Jäggi et al. 2023). The surfaces of these airless planetary bodies are covered in a regolith that has been space-weathered by SW ion sputtering, photon-stimulated desorption, and thermal desorption (B. Hapke 2001; C. J. Bennett et al. 2013; D. L. Domingue et al. 2014; C. M. Pieters & S. K. Noble 2016). These processes all affect the top 50–100 nm of the regolith grains, altering the surface elemental composition and crystallinity from that of the bulk. Micrometeoroid impact vaporization and gardening affect regolith to deeper levels and expose fresh material (Z. Huang et al. 2021; P. Wurz et al. 2022). As a result, exposed grain surfaces can contain mineral and amorphous fractions, elementally pure nano-phase regions of iron or other elements, and agglutinates. Our focus here is on ion sputtering of mineral fractions, particularly plagioclase feldspars. Returned lunar samples have suggested that plagioclase feldspars (a solid solution of albite and anorthite), are abundant on the lunar surface (G. Heiken et al. 1991; J. Papike et al. 1991) Mercury observations also suggest that the surface is abundant in intermediate composition plagioclase feldspars (J. Papike et al. 1991; A. L. Sprague et al. 2002; D. L. Domingue et al. 2014;

P. N. Peplowski et al. 2014; W. E. McClintock et al. 2018; T. J. McCoy et al. 2018).

Planetary scientists modeling space weathering take much of the needed ion-sputtering parameters (P. Wurz et al. 2022) from binary collision approximation (BCA) models, which treat sputtering as the result of a cascade of binary collisions of atomic nuclei (W. Eckstein & H. M. Urbassek 2007). Early BCA models were presented by M. W. Thompson (1968) and P. Sigmund (1969). More recently used in planetary science today is the extended version of the BCA Monte Carlo code Transport Range of Ions in Matter (TRIM; J. F. Ziegler & J. P. Biersack 1985) known as SDTrimSP (A. Mutzke et al. 2019), which can be run in standard (S) or dynamical (D) mode (the latter of which tracks compositional changes in the impacted substrate) using either serial (S) or parallel (P) processing. SDTrimSP is a BCA model to predict the ejecta energy distribution, sputtering yield, and angular distribution of sputtered atoms as a function of the impacting ion type, energy, and impact angle. SDTrimSP has been shown to be more reliable than TRIM at impact energies relevant to solar wind ions (Hofsäss et al. 2014).

A fundamental input parameter for these BCA models is the surface binding energy (SBE) of each element in the impacted substrate (R. Kelly 1986; R. Behrisch & W. Eckstein 2007). The SBE is the minimum energy along the surface normal that is required for an atom to be completely removed from the surface. The SBE determines the yield and energy distribution of the ejecta (M. W. Thompson 1968; P. Sigmund 1969). In our past studies of SW sputtering on the Moon and Mercury, we demonstrated that discrepancies in the SBE can have a significant effect on the calculated SW-ion-induced sputtering yield and the resulting predicted exosphere (R. M. Killen et al. 2022; L. S. Morrissey et al. 2022b, 2023).

Most of the current simulation tools for ion sputtering assume that the SBE is independent of the substrate composition or atomic arrangement and that the SBE can be approximated as the mono-elemental sublimation energy, namely equal to the cohesive energy for the ground state of an individual atom in a mono-elemental substrate (K. A. Gschneidner 1964; R. Behrisch & W. Eckstein 2007). For example, SDTrimSP recommends using the mono-elemental cohesive energy for each element in an unstructured compound (A. Mutzke et al. 2019), thus assuming that the SBE of an atom is independent of the bonds formed with other, different elements in the compound. However, planetary surfaces are not elementally pure. Rather, they contain a range of multi-elemental materials in both crystalline and amorphous forms. A complete understanding is lacking for the SBEs of the different species from these multielemental substrates.

Recent studies have attempted to constrain the SBE of different elements in minerals based on best-fitting simulated sputtering yields to experimental total mass measurements. M. J. Schaible et al. (2017) considered only the O SBE in SDTrimSP and derived values between 1 and 3 eV based on comparison to experimental total sputtering yields of silica. P. S. Szabo et al. (2020) considered a compound SBE and derived an O SBE of 6.5 eV based on fitting to experimental total sputtering yields of wollastonite (CaSiO_3). As an alternative, N. Jäggi et al. (2023) developed a hybrid model that combines a surface binding approach with a bulk binding model. This approach considers an atom in a mineral to be either chemically bound in its preferred oxide/sulfide or “free”

(unbound) and thus able to move throughout the mineral. A limitation of all these models is that the predicted sputtering yields were only benchmarked against total mass sputtering measurements. Therefore, these models will not necessarily accurately predict the elemental composition of the sputtering yield and may also be discrepant in the predicted energy distribution of the ejecta. A further limitation of these three approaches is their inability to investigate how the individual elemental sputtering yields vary as the corresponding SBEs change as the substrate weathers.

As an alternative to these approaches, molecular dynamics (MD) simulations can be used to directly calculate SBEs for different substrate compositions. This has been well established for mono-elemental metals (H. Gades & H. M. Urbassek 1994; D. P. Jackson 1973, 1975; X. Yang & A. Hassanein 2014a; L. S. Morrissey et al. 2021) and Si-bearing compounds (S. Bringuier et al. 2019). Previously, we have used MD simulations to model the SBE of Na from silicates, including the plagioclase feldspar endmember albite (L. S. Morrissey et al. 2022b). The MD-calculated Na SBE from albite was 7.9 eV, significantly higher than the Na cohesive energy of 1.1 eV, and in reasonable agreement with the limited experimental measurements of the ejecta energy distribution (C. A. Dukes & R. A. Baragiola 2015). These combined results suggest that SBEs are mineral-specific and cannot be assumed to be independent of the bonds formed on the surface.

MD can also be used to simulate ion sputtering, but the significant calculational cost renders this approach computationally unfeasible for sputtering yield studies. A more tractable approach is to use MD-derived SBEs for elements from specific compounds as inputs into the more computationally efficient BCA models to predict ion-sputtering behavior. When used as an input into SDTrimSP, our MD-derived Na SBE from albite decreased the Na sputtering yield by a factor of 15 (as compared to the cohesive energy approximation) and had a significant effect on the fraction of sputtered Na atoms exceeding the escape energy for Na from the gravity wells of the Moon and Mercury (L. S. Morrissey et al. 2022b). However, in that study we only simulated ion sputtering of one element (Na) from one crystalline surface for each of the Na-bearing compounds considered.

The importance of the SBE in understanding SW-ion-induced sputtering has led to several researchers calling for further MD calculations of SBEs relevant to planetary science (H. M. Urbassek 2007; S. Bringuier et al. 2019; L. S. Morrissey et al. 2021 2022b; R. M. Killen et al. 2022; P. Wurz et al. 2022; N. Jäggi et al. 2023). To advance the field, SBEs are needed for all the elements in the relevant compounds for all the expected cleavage planes. Here, we have used MD to calculate the SBE of all element types within crystalline albite and anorthite, the two endmembers of plagioclase feldspars. We have performed calculations for each of the three expected crystalline surfaces of each mineral ((001), (010), and (011), using the Miller indices for surfaces).

The remainder of this paper is as follows: Section 2 presents the MD approach used to calculate the SBEs from the various orientations of the albite and anorthite surfaces. Section 3 presents the mineral-specific SBEs for all elements therein and explores the effect of these SBE values on the predicted sputtering yield and ejecta energy distribution. Section 4 summarizes the findings and discusses future work.

2. Methodology

In this study, we have used MD to quantify the SBEs of all elements in albite ($\text{NaAlSi}_3\text{O}_8$) and anorthite ($\text{CaAl}_2\text{Si}_2\text{O}_8$), the two endmembers of the plagioclase feldspar group. For each mineral, we developed and equilibrated the three cleavage planes in MD. We then used MD to determine how the crystal orientation of the exposed plane affects the SBE of each element type. These MD-derived SBEs were then used as inputs into BCA models to predict their effects on the subsequent sputtering behavior. We note that here we have only considered the fundamental cases of crystalline minerals and not amorphous substrates or those that have been dynamically weathered. Our work here is an important first step to understanding how SBEs can vary for weathered samples on the surfaces of airless bodies.

2.1. Molecular Dynamics Simulations

MD simulations were performed using the Large-scale Atomic/Molecular Massively Parallel Simulation (LAMMPS) package (S. J. Plimpton 1995; A. P. Thompson et al. 2022). Interactions between atoms in each mineral were simulated using a reactive force field (ReaxFF) empirical potential that allows for the dynamic simulation of bond breaking and reformation in a multielemental substrate (A. C. T. Van Duin et al. 2001). ReaxFF is uniquely able to simulate both bonded and nonbonded interactions. Connectivity-dependent reactions (valence and torsion energy) are modeled so that when bonds are broken their contribution to the total energy is zero. Nonbonded, van der Waals, and long-range Coulomb interactions are calculated irrespective of the connections between all atom pairs in the simulation. As a result, ReaxFF potentials do not require the use of long-range interaction methods such as those of Ewald (P. P. Ewald 1921) or D. Wolf et al. (1999). Coulomb interactions are cut off at a standard distance of 10 Å. More details are given in A. C. T. Van Duin et al. (2001). For our study, we selected a ReaxFF potential developed by M. C. Pitman & A. C. T. Van Duin, (2012) and modified by G. A. Lyngdoh et al. (2019) for structures composed of Na, Ca, Al, Si, and O. This potential has been validated for a range of crystalline silicate structures, including albite but not anorthite, and has been shown to provide accurate descriptions of both bulk and surface properties (G. A. Lyngdoh et al. 2019).

2.1.1. Developing and Equilibrating Mineral Substrates

We performed MD simulations for each mineral using the perfect (001), good (010), and imperfect (110) cleavage planes (J. W. Anthony et al. 2001). We first used MD to develop and equilibrate model crystalline substrates containing approximately 2500–4900 atoms, depending on the mineral and surface simulated. For the (001) and (010) surfaces, we replicated the mineral’s conventional unit cell from the Materials Project database (A. Jain et al. 2013): 5 times in the x direction (41.7 Å wide), 5 times in the y direction (29.9 Å wide), and 3 times in the z direction (50.5 Å thick). For the (110) surface, we used the slab builder in Avogadro (M. D. Hanwell et al. 2012) to generate a substrate with the (110) surface oriented along the z direction (48.4 Å wide in x and y , and 20.2 Å thick in z). Each substrate then underwent a charge equilibration using the electron equilibration method approach (W. J. Mortier et al. 1986) as implemented in LAMMPS (S. J. Plimpton 1995) and described by A. C. T. Van Duin et al. (2001). The equilibration

minimized the electrostatic energy by adjusting partial charges on individual atoms based on neighbor interactions. Next, a Berendsen barostat and then a Berendsen thermostat (H. J. C. Berendsen et al. 1984) were used to relax each substrate and equilibrate it to 1 K and 0 atm (the simulated condition) using MD. The simulation domain was then extended 100 Å in the z direction above the surface of interest. Boundary conditions were fixed in the direction normal to the surface of interest and periodic along the lateral directions, simulating an infinite slab with constant thickness and a free surface. Atoms in the bottom three angstroms in the fixed direction of each substrate were fixed in space.

2.1.2. Determining the Surface Structure

Figures 1 and 2 show the atomic arrangement of the (001), (010), and (110) planes exposed at the surface of the albite and anorthite substrate. These figures also show that a single constituent element can occupy multiple repeating positions at the surface, and each of these repeating surface positions (SPs) has its own unique chemical bonds and nearest neighbor atoms. We used MD to calculate the SBE for every possible repeating SP that each given element could occupy. Because there is no consistently adopted method for identifying surface atoms from bulk atoms of the atomic scale (F. Deanda & R. S. Pearlman 2002), we defined surface atoms as those that were readily exposed on the specified cleavage plane and were within the first 2 Å of the surface. We have selected this depth guided by previous SDTrimSP simulations that indicate the bulk of the atoms sputtered by solar wind ions come from within the first few angstroms of the surface (L. S. Morrissey et al. 2023). We also note that the sputtering yield decreases as $1/\text{SBE}$ (R. Behrisch & W. Eckstein 2007). So, the increasing SBE with increasing depth that we report below and the corresponding decreasing sputtering yield with increasing depth combine to reduce the effects of the uncertainty in the transition from surface atoms to bulk atoms.

Similar to previous methods (X. Yang & A. Hassanein 2014; S. Bringuier et al. 2019; L. S. Morrissey et al. 2021, 2022b), each surface atom studied was given a specific velocity perpendicular to the surface and its subsequent position and remaining energy were tracked versus time. An iterative method was used to determine the minimum energy needed to remove the surface atom completely from the surface such that it no longer interacted with the surface, i.e., it experienced no attractive or repulsive forces. Because every repeating SP was considered, the probability of each SP in the unit cell was also naturally accounted for.

2.2. BCA Model Simulations

The outputs of the MD simulations were then used as inputs into the BCA SDTrimSP and Thompson models to study the effect of the SBEs on the predicted sputtering yield of the ejecta and corresponding energy distribution. We used SDTrimSP to investigate the sputtering yield for each element type and SBE. SDTrimSP takes the SBE and atomic concentration of each atom type in the overall compound as an input. In SDTrimSP we have defined every SP as a different “atom type” with a unique SBE. The probability for an SP to occur for a given element is equal for all SPs of that element. For a given element type the sum of the probabilities of all the different SPs

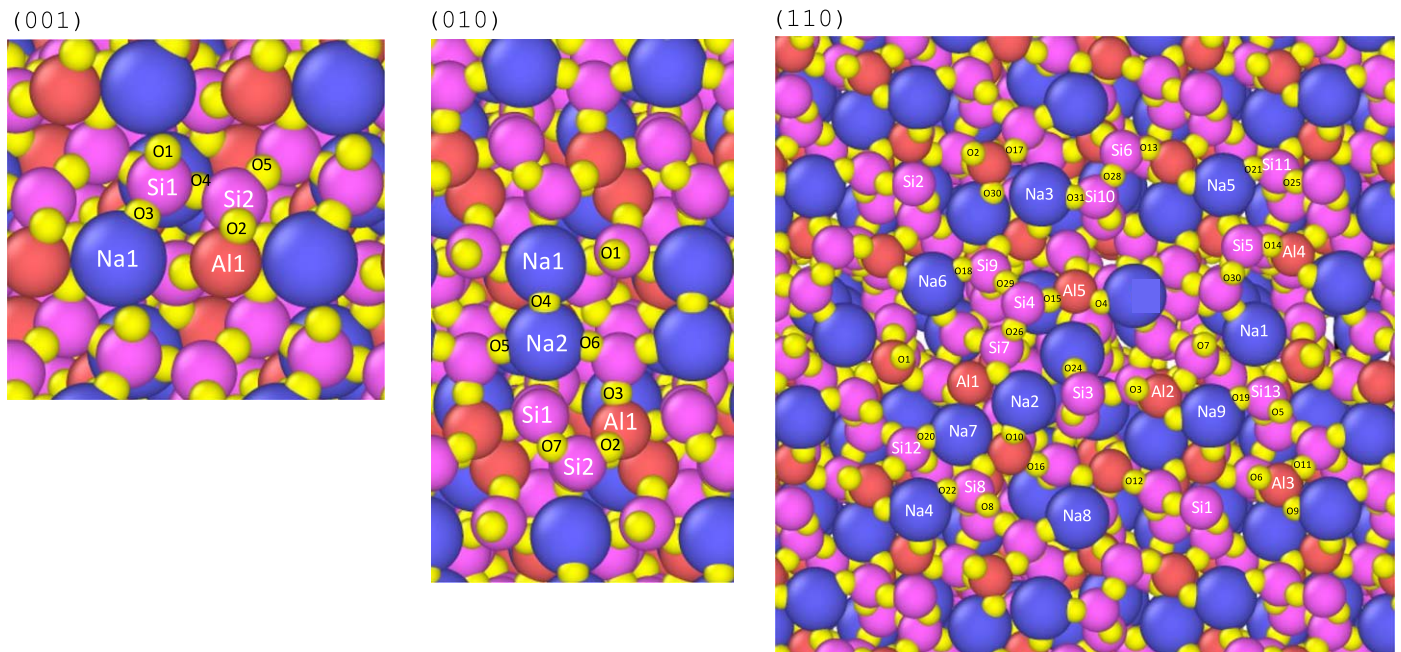


Figure 1. Albite SPs for each element type from the (001), (010), and (110) surfaces. The images are oriented so the $+z$ direction comes out of the page and show a subsection of the complete surface simulated. Sodium atoms are in blue, aluminum atoms are in red, silicon atoms are in pink, and oxygen atoms are in yellow. Each elemental species is numbered by its SP. The spheres representing each element are scaled based on the corresponding atomic radii. The figures were created using the OVITO visualizer for MD simulations (A. Stukowski 2009).

matched the bulk concentration of that element in the compound.

To investigate the ejecta energy distribution for each element type as a function of the SBE, we used the M. W. Thompson, (1968) model, which predicts the probability distribution for the energy of the sputtered ejecta (normalized such that the total probability is one) as

$$P(E) = \frac{1}{2E_b} \frac{E}{(E + E_b)^3}. \quad (1)$$

Here, E is the kinetic energy of the sputtered atom and E_b is the SBE of the sputtered atom. This distribution peaks at $E_b/2$. At high emission energies ($E \gg E_b$), the distribution follows an E^{-2} power law. This distribution has been used in several different exosphere models (R. M. Killen et al. 2004, 2022; M. H. Burger et al. 2010; F. Leblanc et al. 2022), likely because of its simplicity as it depends only on the SBE and is not dependent on the incident ion. P. Sigmund (1969) derived a more realistic model that considered the maximum energy that can be transferred in a binary collision, resulting in a high-energy cutoff for the ejecta energy distribution (H. Lammer et al. 2003; P. Wurz et al. 2022). The Sigmund distribution is a function of the impacting ion energy and mass and the ejected atom SBE and mass, adding several levels of complexity for models of ion sputtering by the multiple species in the SW impacting the multielemental planetary regoliths. Here, we begin to explore the impact of our new SBEs using the Thompson model. In a future work, we will explore their impact using the more complicated Sigmund distribution.

We simulated three different compositions of 1 keV amu^{-1} impactors onto the substrate: 100% H, 100% He, and 96% H + 4% He. These cases represent the two major components of the solar wind along with the solar wind composition recommended by SDTrimSP best practices (L. S. Morrissey et al. 2023).

Results from 100% H and 100% He can be scaled to create other intermediate compositions of the solar wind. In each case, the impactors hit the surface with a cosine distribution of impact angles, to approximate spherical grains (T. A. Cassidy & R. E. Johnson 2005; L. S. Morrissey et al. 2023). For the substrate, we simulated both albite and anorthite, with the elemental composition of each component in the substrate set to the initial bulk elemental ratio for that mineral. The SBE for each element type and corresponding lattice SP were fixed using our MD-derived values. Building on previous studies (P. S. Szabo et al. 2018; L. S. Morrissey et al. 2023), the mass density of O in the mineral was modified in SDTrimSP to achieve the experimentally measured bulk density for the relevant mineral (J. W. Anthony et al. 2001). Note that the stoichiometry of the mineral was not changed. A total of 10^6 impacts were simulated for each case onto a 3000 \AA thick amorphous slab. This thickness is much larger than the penetration depth of the incident H or He impactors, $\sim 150 \text{ \AA}$ and 400 \AA , respectively (L. S. Morrissey et al. 2022a). For each simulated case we tracked the sputtering yield and the composition and energy of the sputtered ejecta.

SDTrimSP simulations can be run either in static or dynamic mode. Static simulations reset the substrate after every impact. This leads to a preferential sputtering of elements with lower SBEs compared to elements with higher SBEs in the substrate. Dynamic simulations allow the substrate composition to change with fluence and depth. This leads to sputtering that evolves to a steady-state stoichiometric at high fluences (M. J. Schaible et al. 2017; L. S. Morrissey et al. 2023). However, previous research has shown nonstoichiometric steady-state yields from regolith-like samples (L. P. Keller & D. S. McKay 1997; J. M. Christoph et al. 2022; L. C. Chaves et al. 2023). Those results suggest a mechanism that replenishes the preferentially sputtered element types at the surface, suggesting a situation closer to the SDTrimSP static mode. The most likely replenishment mechanism is diffusion

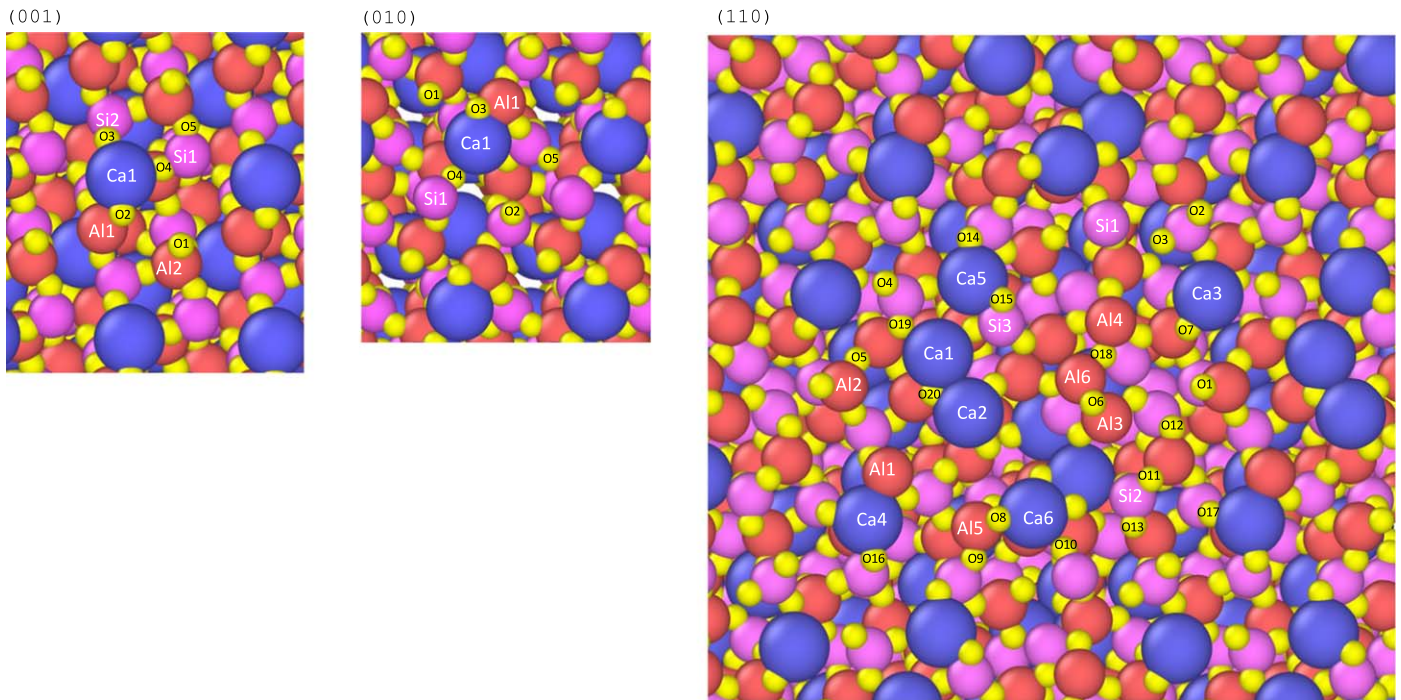


Figure 2. Anorthite SPs for each element type from the (001), (010), and (110) surfaces. The images are oriented so the $+z$ direction comes out of the page and show a subsection of the complete surface simulated. Calcium atoms are in blue, aluminum atoms are in red, silicon atoms are in pink, and oxygen atoms are in yellow. Each elemental species is numbered by its SP. The spheres representing each element are scaled based on the corresponding atomic radii. The figures were created using the OVITO visualizer for MD simulations (A. Stukowski 2009).

(R. A. Yund 1983; B. J. Gilletti & T. M. Shanahan 1997; D. J. Cherniak 2010). However, while diffusion can be added to dynamic SDTrimSP models, the effect of irradiation and implantation on diffusion coefficients for the different element types in silicates have yet to be reliably implemented into BCA modeling (P. S. Szabo et al. 2018, 2020; J. Schmitz et al. 2019). Based on all these considerations, only static simulations were conducted for the present study which allows for preferential sputtering at high fluences, unlike dynamics simulations. Further work is needed to understand the replenishment mechanisms of irradiated minerals.

3. Results and Discussion

3.1. SBEs from MD Simulations

The MD SBEs for albite and anorthite at each cleavage surface are given in Tables 1 and 2, respectively. The SBE was calculated for all possible SPs as a function of the element type and surface orientation. There were 81 and 53 total SPs for all surfaces of albite and anorthite, respectively. For each surface and for a given element, there were significant differences in the SBE as the SP varied. For example, Na atoms from the albite (110) surface have an SBE ranging from 6.5 to 10 eV. We attribute the differences in these SBEs to the different bonds formed by the Na atom at each of the nine available SPs. Similar behavior was observed for anorthite surfaces. For example, for the (110) surface, the Ca SBE ranged from 8.1 to 14.8 eV, depending on which of the six SPs was considered.

For both minerals, the SBEs for all element types were also dependent on the orientation of the surface studied. For example, for O in the (001) and (010) albite surfaces, the SBEs ranged from 7.5 to 16.8 eV (5 different SPs) and 3.3–13.6 eV (7 different SPs), respectively. However, for the imperfect

(110) cleavage plane, there were significantly more SPs (32) and the O SBE ranged from 5.3 to 15.5 eV. Similarly, for anorthite, the SBEs were again dependent on the orientation of the surface. For Al in the (001) surface, there were two SPs (17.3 and 37.6 eV). For the (110) surface, there were six different Al SPs with SBEs ranging from 13.1 to 28.0 eV.

The highest SBEs were consistently seen for the Si and Al, which existed “lower” on the surface and had several bonds. These bonds can be partial contributions from different neighbors and bond types, including O atoms positioned “above” the atom in question. However, in these cases (for example, Si1 in (001) albite) the sputtering of the “lower” Si or Al atom did not remove the terminal O atom “above” it. The SBEs for these atoms are almost an order of magnitude higher than their monoatomic cohesive energies. The monoatomic cohesive energy is commonly used as the input in SDTrimSP but lacks physical relevance to silicates and minerals. In contrast, the lowest SBEs for Al and Si were found when the SP was not terminated “above” by an O atom, for example, the SPs Si3 in (110) albite and Si1 in (110) anorthite. For the higher-SBE SPs, if the “above” O were sputtered first, we expect that the SBE would subsequently decrease closer to these lower values. We suggest that the lowest SBE for each element type in the mineral could be used to approximate the SBEs of a dynamically weathered sample where the lower-SBE atoms (often terminating the higher-SBE atoms) are first removed. In a future study, we will improve this approximation by considering how the SBE can dynamically change as a surface is weathered.

In summary, the SBE for an atom depends on the number, type, and strength of the bonds that it makes with its various neighbors. Altogether, our results demonstrate that the SBE of a given element in a crystalline mineral is not a singular value

Table 1

SDTrimSP-computed Sputtering Yields for the Three Different Impacting Ion Cases as a Function of the Cleavage Plane, Element, SP, and SBE for Albite

Surface	Element	SP	SBE (eV)	Sputtering Yield (atoms/ion)			
				100% H	100% He	96% H + 4% He	
(001)	Na	Na1	8.1	1.51E-03	1.31E-02	1.98E-03	
		Al	Al1	22.3	2.23E-04	5.20E-03	4.17E-04
		Si	Si1	25.0	2.50E-04	7.24E-03	5.24E-04
		...	Si2	28.0	1.78E-04	6.50E-03	4.32E-04
		O	O1	7.5	3.22E-03	2.47E-02	4.11E-03
		...	O2	12.5	1.68E-03	1.63E-02	2.23E-03
		...	O3	9.8	2.26E-03	1.98E-02	3.02E-03
		...	O4	16.8	1.09E-03	1.28E-02	1.53E-03
		...	O5	16.4	1.14E-03	1.31E-02	1.53E-03
	(010)	Na	Na1	4.1	1.84E-03	1.18E-02	2.25E-03
		Na2	10.7	5.21E-04	5.03E-03	7.03E-04	
		Al	Al1	32.0	8.10E-05	3.87E-03	2.26E-04
		Si	Si1	18.8	3.33E-04	6.21E-03	5.71E-04
		...	Si2	26.8	1.31E-04	4.64E-03	2.98E-04
		...	Si3	32.8	6.40E-05	3.68E-03	2.10E-04
		O	O1	6.5	2.76E-03	1.98E-02	3.42E-03
		...	O2	13.6	1.05E-03	1.07E-02	1.45E-03
		...	O3	12.0	1.25E-03	1.21E-02	1.71E-03
		...	O4	3.3	6.17E-03	3.61E-02	7.42E-03
(110)	Na	Na1	10.0	1.60E-03	1.38E-02	2.08E-03	
		Na2	9.8	1.64E-03	1.40E-02	2.12E-03	
		Na3	11.3	1.35E-03	1.23E-02	1.80E-03	
		Na4	10.0	1.28E-04	1.23E-03	1.72E-04	
		Na5	6.5	2.29E-04	1.80E-03	2.97E-04	
		Na6	8.8	1.48E-04	1.37E-03	2.06E-04	
		Na7	8.4	1.56E-04	1.41E-03	2.20E-04	
		Na8	7.5	1.93E-04	1.54E-03	2.45E-04	
		Na9	9.3	1.44E-04	1.27E-03	1.84E-04	
		Na10	8.3	1.56E-04	1.40E-03	2.16E-04	
	Al	Al1	8.0	1.66E-04	1.46E-03	2.22E-04	
	...	Al2	8.4	1.65E-04	1.40E-03	2.12E-04	
	...	Al3	19.3	5.80E-05	1.20E-03	1.08E-04	
	...	Al4	28.0	2.50E-05	8.49E-04	5.79E-05	
	...	Al5	25.0	3.20E-05	9.47E-04	6.78E-05	
	...	Al6	31.0	1.70E-05	7.83E-04	4.38E-05	
	...	Al7	26.0	3.00E-05	9.32E-04	6.54E-05	
	Si	Si1	18.5	7.80E-05	1.47E-03	1.31E-04	
	...	Si2	17.5	8.70E-05	1.55E-03	1.48E-04	
	...	Si3	12.5	1.71E-04	2.06E-03	2.46E-04	
	...	Si4	23.4	4.70E-05	1.21E-03	8.84E-05	
	...	Si5	29.0	2.40E-05	9.93E-04	6.05E-05	
	...	Si6	26.0	3.50E-05	1.09E-03	7.01E-05	
	...	Si7	35.3	1.20E-05	8.26E-04	4.65E-05	
	...	Si8	28.5	2.60E-05	1.00E-03	6.50E-05	
	...	Si9	29.8	2.00E-05	9.69E-04	5.14E-05	
	...	Si10	35.0	1.40E-05	8.13E-04	4.86E-05	
	...	Si11	32.0	1.90E-05	9.02E-04	5.21E-05	
	...	Si12	29.0	2.30E-05	9.82E-04	6.21E-05	
	...	Si13	29.8	2.40E-05	9.52E-04	5.70E-05	
	O	O1	5.3	7.72E-04	5.19E-03	9.27E-04	
	...	O2	5.9	6.78E-04	4.67E-03	8.41E-04	
	...	O3	7.2	5.29E-04	3.91E-03	6.68E-04	
	...	O4	9.8	3.61E-04	3.09E-03	4.68E-04	
	...	O5	8.0	4.61E-04	3.63E-03	6.01E-04	
	...	O6	6.5	5.99E-04	4.31E-03	7.49E-04	
	...	O7	6.4	6.06E-04	4.34E-03	7.65E-04	
	...	O8	7.9	4.67E-04	3.72E-03	6.01E-04	
	...	O9	8.0	4.72E-04	3.66E-03	6.02E-04	
	...	O10	7.1	5.29E-04	4.06E-03	6.87E-04	
	...	O11	13.0	2.39E-04	2.39E-03	3.34E-04	

Table 1

(Continued)

Surface	Element	SP	SBE (eV)	Sputtering Yield (atoms/ion)		
				100% H	100% He	96% H + 4% He
	...	O12	12.0	2.78E-04	2.63E-03	3.80E-04
	...	O13	14.0	2.19E-04	2.29E-03	3.08E-04
	...	O14	13.6	2.19E-04	2.35E-03	3.18E-04
	...	O15	14.6	2.12E-04	2.23E-03	2.86E-04
	...	O16	13.8	2.17E-04	2.32E-03	3.08E-04
	...	O17	14.2	2.10E-04	2.32E-03	2.99E-04
	...	O18	10.4	3.28E-04	2.94E-03	4.28E-04
	...	O19	9.8	3.60E-04	3.03E-03	4.60E-04
	...	O20	8.8	4.16E-04	3.38E-03	5.18E-04
	...	O21	9.1	4.04E-04	3.28E-03	5.11E-04
	...	O22	9.5	3.71E-04	3.16E-03	4.84E-04
	...	O23	8.3	4.36E-04	3.54E-03	5.64E-04
	...	O24	10.9	3.15E-04	2.83E-03	4.11E-04
	...	O25	14.0	2.12E-04	2.29E-03	3.06E-04
	...	O26	15.5	1.99E-04	2.12E-03	2.75E-04
	...	O27	13.3	2.32E-04	2.42E-03	3.25E-04
	...	O28	13.1	2.40E-04	2.43E-03	3.34E-04
	...	O29	15.5	1.86E-04	2.14E-03	2.57E-04
	...	O30	12.1	2.64E-04	2.59E-03	3.57E-04
	...	O31	10.0	3.52E-04	3.07E-03	4.48E-04
	...	O32	8.6	4.22E-04	3.45E-03	5.35E-04

but is instead dependent on the mineral type, SP, and surface orientation.

3.2. Effect on Predicted Sputtering Behavior

3.2.1. Sputtering Yield

BCA sputtering theory was used to study the effect of these MD-derived SBEs on the predicted sputtering behavior. Tables 1 and 2, respectively, provide the sputtering yields from SDTrimSP for albite and anorthite from each elemental SP for each surface orientation and impacting ion case. Tables 3 and 4, respectively, provide the elemental sputtering yields (Y^X) for each element X from albite and anorthite surfaces. The total elemental sputtering yield is given by:

$$Y^X = \sum_{SP} Y_{SP}^X \quad (2)$$

Here, Y_{SP}^X is the sputtering yield for a given element and SP. For all cases, the sputtering yield is highly preferential and nonstoichiometric, favoring the lower-SBE atoms. If no replenishment occurs this would eventually lead to a nonstoichiometric surface depleted in the loosely bound SBEs. In all cases, there is a reduction in the yield with increasing SBE, meaning that SPs with a high SBE contribute less to the elemental yield than those with lower SBEs. As expected, in all cases, the lowest yields were for 100% H cases and the highest yields were observed for the 100% He cases.

We note that when a solar wind composition of 96% H and 4% He is considered, there is an increase in the overall and elemental yields relative to the pure H case. However, this increase is not uniform for the different element types considered. The yield of Na from albite increases by a factor of ≈ 1.3 for the different surface orientations of albite.

Table 2

SDTrimSP-computed Sputtering Yields for the Three Different Impacting Ion Cases as a Function of the Cleavage Plane, Element, SP, and SBE for Anorthite

Surface	Element	SP	SBE (eV)	Sputtering Yield (atoms/ion)		
				100% H	100% He	96% H + 4% He
(001)	Ca	Ca	14.3	3.46E-04	7.04E-03	6.25E-04
	Al	Al1	17.3	3.80E-04	6.64E-03	6.30E-04
	...	Al2	37.6	4.44E-05	3.30E-03	1.73E-04
	Si	Si1	22.0	2.24E-04	5.53E-03	4.42E-04
	...	Si2	35.5	4.53E-05	3.41E-03	1.90E-04
...	O	O1	5.7	4.54E-03	3.15E-02	5.48E-03
	...	O2	8.3	2.81E-03	2.32E-02	3.60E-03
	...	O3	11.0	1.94E-03	1.80E-02	2.58E-03
	...	O4	14.5	1.30E-03	1.45E-02	1.86E-03
	...	O5	14.5	1.32E-03	1.46E-02	1.84E-03
(010)	Ca	Ca	13.5	4.00E-04	7.46E-03	7.18E-04
	Al	Al	18.0	7.27E-04	1.30E-02	1.19E-03
	Si	Si	15.0	1.06E-03	1.57E-02	1.17E-03
	O	O1	6.0	4.26E-03	2.99E-02	5.11E-03
	...	O2	7.0	3.54E-03	2.64E-02	4.36E-03
(110)	...	O3	8.0	2.61E-03	2.19E-02	3.43E-03
	...	O4	13.8	1.44E-03	1.51E-02	1.92E-03
	...	O5	12.9	1.56E-03	1.61E-02	2.13E-03
	Ca	Ca1	8.1	1.85E-04	1.94E-03	2.52E-04
	...	Ca2	12.3	8.63E-05	1.34E-03	1.34E-04
	...	Ca3	10.3	1.24E-04	1.58E-03	1.82E-04
	...	Ca4	14.3	5.65E-05	1.21E-03	1.04E-04
	...	Ca5	14.8	5.86E-05	1.16E-03	1.03E-04
	...	Ca6	13.8	6.06E-05	1.32E-03	1.13E-04
	Al	Al1	13.1	2.28E-04	2.95E-03	3.27E-04
...	...	Al2	24.0	6.06E-05	1.67E-03	1.29E-04
	...	Al3	15.3	1.67E-04	2.59E-03	2.61E-04
	...	Al4	17.0	1.39E-04	2.31E-03	2.19E-04
	...	Al5	28.0	3.91E-05	1.57E-03	9.69E-05
	...	Al6	19.8	9.35E-05	2.10E-03	1.73E-04
	Si	Si1	17.8	2.54E-04	4.57E-03	4.12E-04
	...	Si2	24.8	1.05E-04	3.44E-03	2.46E-04
	...	Si3	19.8	1.98E-04	4.12E-03	3.67E-04
	O	O1	6.8	8.49E-04	6.70E-03	1.10E-03
	...	O2	7.9	7.34E-04	5.84E-03	9.25E-04
	...	O3	9.3	6.20E-04	5.20E-03	7.81E-04
	...	O4	8.0	7.01E-04	5.78E-03	9.32E-04
	...	O5	12.8	3.81E-04	3.96E-03	5.43E-04
	...	O6	7.6	8.01E-04	6.09E-03	9.79E-04
	...	O7	8.0	7.15E-04	5.99E-03	9.31E-04
	...	O8	6.3	9.59E-04	7.16E-03	1.22E-03
	...	O9	13.2	3.65E-04	3.97E-03	5.18E-04
	...	O10	12.9	3.86E-04	3.99E-03	5.31E-04
	...	O11	12.4	4.01E-04	4.09E-03	5.40E-04
	...	O12	13.0	3.69E-04	3.93E-03	5.09E-04
...	O13	14.3	3.33E-04	3.58E-03	4.53E-04	
...	O14	10.6	5.01E-04	4.67E-03	6.59E-04	
...	O15	11.1	4.57E-04	4.36E-03	6.23E-04	
...	O16	9.6	5.59E-04	5.07E-03	7.31E-04	
...	O17	10.6	4.99E-04	4.70E-03	6.66E-04	
...	O18	13.0	3.69E-04	3.91E-03	5.14E-04	
...	O19	13.3	3.61E-04	4.01E-03	5.22E-04	
...	O20	10.7	4.94E-04	4.63E-03	6.52E-04	

However, the yield of Al from albite is increased by a factor of 1.9–2.8 for the different surfaces. We attribute these differences to the increased efficiency of 4 keV He ions in ejecting the more tightly bound SPs. For example, the yield of the surface position “Si7” from (110) albite (the highest SBE SP) is

Table 3

SDTrimSP-computed Elemental Sputtering Yields from Albite for the Three Different Impacting Ion Cases as a Function of the Cleavage Plane Using All SP SBEs

Surface	Element	Sputtering Yield (atoms/ion)		
		100% H	100% He	96% H + 4% He
(001)	Na	1.51E-03	1.31E-02	1.98E-03
	Al	2.23E-04	5.20E-03	4.17E-04
	Si	4.28E-04	1.37E-02	9.56E-04
	O	9.38E-03	8.67E-02	1.24E-02
(010)	Na	2.36E-03	1.69E-02	2.95E-03
	Al	8.10E-05	3.87E-03	2.26E-04
	Si	5.28E-04	1.45E-02	1.08E-03
(110)	O	1.58E-02	1.19E-01	2.00E-02
	Na	1.49E-03	1.29E-02	1.97E-03
	Al	1.62E-04	4.71E-03	3.43E-04
	Si	5.80E-04	1.48E-02	1.13E-03
...	O	1.18E-02	9.98E-02	1.54E-02

Note. The maximum error due to counting statistics is 10%.

Table 4

SDTrimSP-computed Elemental Sputtering Yields from Anorthite for the Three Different Impacting Ion Cases as a Function of the Cleavage Plane Using All SP SBEs

Surface	Element	Sputtering Yield (atoms/ion)		
		100% H	100% He	96% H + 4% He
(001)	Ca	3.46E-04	7.04E-03	6.25E-04
	Al	4.24E-04	9.94E-03	8.03E-04
	Si	2.69E-04	8.94E-03	6.32E-04
	O	1.19E-02	1.02E-01	1.54E-02
(010)	Ca	4.00E-04	7.46E-03	7.18E-04
	Al	7.27E-04	1.30E-02	1.19E-03
	Si	1.06E-03	1.57E-02	1.17E-03
(110)	O	1.34E-02	1.09E-01	1.69E-02
	Ca	5.72E-04	8.55E-03	8.88E-04
	Al	7.27E-04	1.32E-02	1.20E-03
	Si	5.57E-04	1.21E-02	1.03E-03
...	O	1.09E-02	9.76E-02	1.43E-02

Note. The maximum error due to counting statistics is 10%.

increased by a factor of 3.9 when 4% He is included. Those surfaces with higher-SBE SPs have a larger difference between the 100% H case and the 96% H + 4% He case. This demonstrates that the He contribution to the elemental sputtering yield by the solar wind cannot be accounted for by multiplying the 100% H results by a single factor but depends on the specific SBE for the different SPs of each element. Instead, the individual results for 100% H and 100% He can be scaled together to create other intermediate compositions of the solar wind.

3.2.2. Energy Distribution of Ejecta

The energy distribution of the sputtered ejecta is needed to determine the altitude distribution of an element in an exosphere, along with the sputtering contribution that exceeds the escape energy of the planetary body. Here, we use the M. W. Thompson (1968) model to demonstrate a methodology for incorporating the various SBEs into exosphere models. The Thompson model was chosen as it is commonly incorporated into preexisting exosphere models to describe the energy

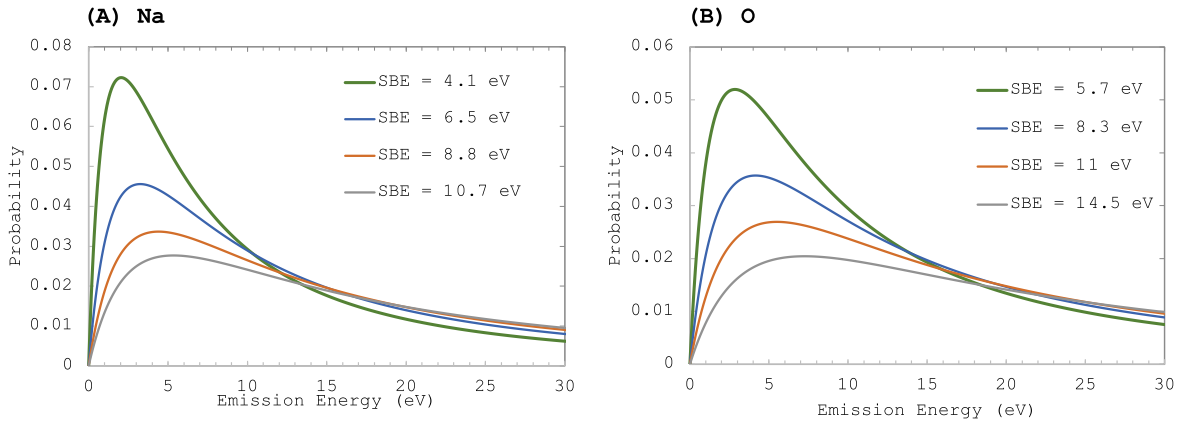


Figure 3 Ejecta emission energy probability distributions using the Thompson model for different SBEs for (A) a sample of Na SPs sputtered from different albite surfaces and (B) for all O SPs sputtered from a (001) anorthite surface.

Table 5

Elemental Best-fit E_b Values (in eV) for the Different Surface Orientations of Albite and Their Agreement to a Sputtering-yield-weighted Thompson Distribution

Surface Orientation		100% H				100% He				96 % H + 4% He			
		Na	Al	Si	O	Na	Al	Si	O	Na	Al	Si	O
(001)	Fit E_b (eV)	8.1	22.3	26.3	10.4	8.1	22.3	26.3	11	8.1	22.3	26.2	10.4
	rms (%)	0.0	0.0	0.3	2.3	0.0	0.0	0.1	2.4	0.0	0.0	0.0	2.3
	Max Error (%)	0.0	0.0	1.2	12.0	0.0	0.0	0.1	14.1	0.0	0.0	0.0	12.0
	Min Error (%)	0.0	0.0	-0.2	-3.6	0.0	0.0	-0.2	-3.6	0.0	0.0	-0.4	-3.6
(010)	Fit E_b (eV)	5.1	32.0	21.5	6.3	5.6	32.0	23.1	7.0	5.1	32.0	22.5	6.7
	rms (%)	3.5	0.0	1.3	6.7	4.2	0.0	2.2	6.5	4.1	0.0	1.2	6.6
	Max Error (%)	19.5	0.0	3.4	40.0	26.7	0.0	1.2	41.3	17.7	0.0	4.7	44.9
	Min Error (%)	-5.4	0.0	-2.0	-12.1	-6.8	0.0	-3.9	-10.4	-5.7	0.0	-1.7	-10.6
(110)	Fit E_b (eV)	8.2	23.5	17.4	8.6	8.3	24.7	22.2	9	8.2	24	18.5	8.8
	rms (%)	0.7	0.9	18.0	4.6	0.8	0.9	33.6	4.6	0.7	0.8	18.1	3.1
	Max Error (%)	4.6	2.7	3.5	3.9	5.7	3.1	2.2	4.8	5.3	3.8	-1.9	6.3
	Min Error (%)	0.2	-1.5	-21.2	-9.5	0.0	-1.3	-36.4	-9.4	-8.0	-0.6	-28.6	-8.7

distribution of SW sputtered atoms. We recognize that this will overestimate the high-energy ejecta. In a future work, we will address this same issue using the more complex distribution from P. Sigmund (1969). For all element types and substrates, the SBE has a significant effect on the energy distribution of the ejecta. Figure 3 gives examples of the ejecta energy distributions for a sample of Na SPs from different albite surfaces (A) and for all O SPs sputtered from the anorthite (001) surface (B). As the SBE increases, the peak shifts to higher energies, and the width of the distribution increases. Increasing the O SBE from 5.7 eV (the lowest SBE for all O SPs in anorthite) to 14.5 eV (the highest SBE for all O SPs in anorthite), increases the peak energy by a factor of 2.5 and the FWHM by a factor of 2.6. These trends are observed for all cases simulated. Clearly, accounting for the different SBEs at each SP will have a significant effect on the energy distribution of the ejecta.

3.2.3. Using Fitting to Predict Energy Distribution of the Ejecta

To enable exosphere modelers to incorporate our MD-SBE values for crystalline plagioclase feldspars without having to explicitly account for 81 and 53 total SPs for albite and anorthite, respectively, we have investigated whether a singular fitting E_b value could be used to predict the ejecta energy distribution from all SPs for a given element type X from a specific surface orientation. Tables 5 and 6 provide the best-fit

E_b values for each element type, surface orientation, and mineral composition. Also given in the tables is the agreement of the fits compared to the corresponding sputtering-yield-weighted summation of each Thompson distribution for all individual SPs of element X . The weighted Thompson probability distribution curves describe the ejecta energy distribution properly accounting for the SBE of each SP. This weighted summation curve was formed by multiplying each ejecta energy distribution by the corresponding relative contribution to the total sputtering yield and then adding the terms together as

$$P^X(E) = \sum_{SP} \frac{1}{2E_{b,SP}^X} \frac{E}{(E + E_{b,SP}^X)^3} \cdot \frac{Y_{SP}^X}{Y^X}. \quad (3)$$

Here, $P^X(E)$ is the probability for a specific emission energy E of element X and $E_{b,SP}^X$ is the SBE for a given SP and element. The sputtering yield for a specific emission energy is then given trivially by:

$$Y^X(E) = Y^X \cdot P^X(E). \quad (4)$$

Using a singular fitting E_b gave excellent agreement to the weighted summation in all cases. Considering the four elements in each of the two minerals, the three surface orientations, and three impactor compositions, a total of 72 cases were considered (Tables 5 and 6). The best-fit value was

Table 6Elemental Best-fit E_b Values (in eV) for the Different Surface Orientations of Anorthite and Their Agreement to a Sputtering-yield-weighted Thompson Distribution

Surface Orientation		100% H				100% He				96 % H + 4% He			
		Ca	Al	Si	O	Ca	Al	Si	O	Ca	Al	Si	O
(001)	Fit E_b (eV)	14.3	18.3	3.5	7.8	14.3	21.2	25.7	9.0	14.3	19.5	24.8	8.6
	rms (%)	0.0	1.3	0.9	3.2	0.0	3.7	1.7	3.3	0.0	2.5	1.5	3.3
	Max Error (%)	0.0	2.9	2.0	8.0	0.0	9.8	4.2	20.5	0.0	5.5	3.3	20.0
	Min Error (%)	0.0	-2.0	-1.4	-6.9	0.0	-5.6	-2.6	-4.9	0.0	-4.0	-2.2	-3.8
(010)	Fit E_b (eV)	13.5	18.0	15.0	7.9	13.5	18.0	15.0	8.2	13.5	18.0	15.0	8.0
	rms (%)	0.0	0.0	0.0	2.1	1.0	1.0	1.0	2.4	0.0	0.0	0.0	2.1
	Max Error (%)	0.0	0.0	0.0	12.1	0.0	0.0	0.0	12.8	0.0	0.0	0.0	12.3
	Min Error (%)	0.0	0.0	0.0	-3.1	0.0	0.0	0.0	-3.6	0.0	0.0	0.0	-3.1
(110)	Fit E_b (eV)	9.4	15.3	19.5	8.7	10.0	16.8	20.1	8.8	9.8	16.0	19.8	8.8
	rms (%)	12.4	16.3	0.8	6.2	16.3	18.8	0.5	7.6	13.7	17.1	0.5	6.4
	Max Error (%)	-4.3	-12.9	1.8	-1.6	-8.0	-13.1	1.8	-1.6	-6.4	13.8	0.7	-2.0
	Min Error (%)	-28.1	-19.8	0.2	-12.2	-32.3	-22.0	-0.8	-16.0	-26.6	-20.3	-1.0	-12.3

Table 7Elemental Best-fit E_b Values for Albite and Anorthite Assuming an Even Probability of the (001), (010), and (110) Surfaces and Their Agreement to a Sputtering-yield-weighted Thompson Distribution That Incorporates All SBEs for the Different SPs

Mineral	Element	100% H				100% He				96% H + 4% He			
		Fit E_b (eV)	rms (%)	Max Error (%)	Min Error (%)	Fit E_b (eV)	rms (%)	Max Error (%)	Min Error (%)	Fit E_b (eV)	rms (%)	Max Error (%)	Min Error (%)
Albite	Na	7.0	2.6	21.5	-3.3	7.2	2.6	21.6	-3.2	6.9	2.5	19.9	-3.2
	Al	28.7	1.1	4.5	-1.4	29.1	0.9	2.8	-1.3	28.8	0.8	3.7	-1.2
	Si	21.7	6.3	7.5	-7.8	21.8	6.4	8.1	-7.7	22.9	7.7	6.9	-9.0
	O	8.2	5.4	32.7	-10.1	8.9	5.1	33.7	-8.7	8.7	5.6	38.4	-8.3
Anorthite	Ca	12.5	2.3	1.5	-4.2	12.8	3.1	-0.3	-4.9	12.6	2.5	0.2	-4.6
	Al	17.3	5.3	-2.2	-6.5	18.8	6.8	2.2	-8.4	18.0	5.9	0.3	-7.2
	Si	18.7	1.2	5.3	-1.8	19.4	2.1	6.6	-3.3	19.1	1.8	5.3	-3.0
	O	8.3	3.0	9.1	-6.2	8.7	3.4	10.0	-6.9	8.5	3.0	12.0	-5.7

determined by minimizing the rms error. The rms error over the first 100 eV of ejection energies was calculated via:

$$\text{rms} = \sqrt{\frac{\sum_{i=1}^N \left(\frac{Y^X(E_i) - Y_{\text{fit}}^X(E_i)}{Y^X(E_i)} * 100 \right)^2}{N}}. \quad (5)$$

Here $N = 1000$ is the number of discrete emission energy data points considered over the first 100 eV and $Y_{\text{fit}}^X(E_i)$ is the sputtering yield calculated using the best-fit value. For albite and anorthite, the rms error in 71 of the 72 cases was less than $\pm 20\%$. The only rms above 20% was for Si sputtered from (110) albite using 100% He impactors (rms of 33.9%). We attribute this larger error in the fits to the factor of ~ 3 spread in the SBE values for the different Si SPs, which significantly affects the elemental yield.

We also developed an approach to derive a singular best-fit E_b for each element type from albite and anorthite assuming an equal probability of the three different surface orientations considered. This approach enables exosphere modelers to more easily incorporate only one SBE for each element type in each mineral. It is important to note that this approach could be used for other SBE distributions (such as those from weathered samples) and is not unique to just the crystalline data set provided here. Table 7 provides the best-fit E_b for each element, along with their agreement compared to the even summation of the curves formed using Equation (3) for each

surface orientation. For all cases, a single E_b value approximated the weighted distribution with excellent agreement. The rms was less than $\pm 8\%$ for all cases considered. Taken together, these results suggest that using a singular best-fit E_b for each element X in a mineral is a suitable approximation for simulating the sputtering yield and energy distribution of the ejecta. Future work is needed to understand the relative probability of different surface orientations being exposed on the surface.

There are limited experimental data available for the sputtering yield of the ejecta from minerals relevant to planetary science. P. S. Szabo et al. (2020) studied the sputtering behavior of crystalline wollastonite (CaSiO_3) exposed to 100% 1 keV H and 100% 4 keV He. Similarly, H. Biber et al. (2022) studied the sputtering behavior of crystalline enstatite (MgSiO_3) exposed to 4 keV He. In both cases, only the total mass yield, and not the composition of the yield, was quantified as a function of the incidence angle. While neither of these minerals match those considered here, they are both silicates and can be used to potentially validate the approach used here. Our results are in good quantitative agreement with the provided experiments. For 1 keV H impacts on anorthite and albite we predict yields of $\sim 0.2\text{--}0.3$ amu ion $^{-1}$, agreeing well with findings from Szabo et al. for H onto Wollastonite ($\sim 0.2\text{--}0.3$ amu ion $^{-1}$). For 4 keV He impacts we predict an approximate order of magnitude increase in the yield to $\sim 2\text{--}3$ amu ion $^{-1}$. Experimental results from Szabo et al. and Biber et al. find yields of between ~ 2 and

5 amu ion⁻¹ for 4 keV He impacts on wollastonite and enstatite. This good agreement provides strong validation for the MD-generated SBEs provided here and the proposed method of incorporating them into SDTrimSP.

3.2.4. Future Considerations for Planetary Science

The results presented here are for the fundamental cases of stoichiometric crystalline minerals and not amorphous substrates or those that have been dynamically weathered by SW. In this case, future studies are needed to understand how the SBE evolves dynamically as the sample becomes weathered (either in the laboratory or due to SW ions) and as the lower-SBE atoms (often terminating the higher-SBE atoms) are removed preferentially. These values are potentially relevant for exosphere models of the Moon and Mercury. In addition, studies are needed comparing elemental yields from SDTrimSP predictions using MD-derived SBEs to experimental results. These studies will provide critically needed benchmarking of the combined MD-SBE/SDTrimSP method proposed here.







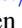



4. Summary

We have used MD to predict elemental SBEs from different crystalline surfaces of albite and anorthite, the endmembers of plagioclase feldspar. Our results show that each SBE is dependent on the surface orientation and SP, meaning that multiple SBEs are possible for a given element within a mineral. Using these MD results, in combination with the commonly used BCA model SDTrimSP, we have predicted the sputtering yield for every SP for every element for all cleavage planes for each mineral. We have considered irradiation by 1 keV amu⁻¹ impactors of 100% H, 100% He, and a solar wind mixture of 96% H + 4% He. We expect that the sputtering yield results from these endmembers can be linearly scaled to intermediate composition plagioclase feldspars, though this remains to be verified experimentally. We also show that including the He components in the solar wind can have a significant effect on the sputtering yield of the higher-SBE SPs, as compared to irradiation by H ions only. We have provided a comprehensive database of SBEs and sputtering yields for the different minerals, surface orientations, elements, and SPs considered, as well as the composition of the impactors. We have also developed an approach to obtain best-fit SBE values for each element type for each cleavage plane of albite and anorthite. We further simplified by averaging over all three possible crystalline orientations and presenting the corresponding best-fit elemental SBE values for albite and anorthite. In our future MD studies, we plan to explore the effects on SBEs due to amorphization of the original mineral and to apply the more complex P. Sigmund (1969) ejecta energy distribution.

Acknowledgments

C.B, M.H.B, D.S.E, G.E.H., R.M.K., D.W.S., and O.J.T were supported, in part, by NASA Solar System Workings Program Award grant No. 80NSCC22K0099. L.M. was supported in part by the NSERC Discovery Grant and the CSA Research Opportunities in Space Sciences program awards. Z.H. and C.D. were supported, in part, by NASA grant 80NSSC23K0894. D.W.S. thanks P. Wurz for stimulating discussions.

ORCID iDs

Liam S. Morrissey  <https://orcid.org/0000-0001-7860-9957>
 Caixia Bu  <https://orcid.org/0000-0002-4426-4425>
 Matthew H. Burger  <https://orcid.org/0000-0002-9334-7198>
 Chuanfei Dong  <https://orcid.org/0000-0002-8990-094X>
 Denton S. Ebel  <https://orcid.org/0000-0003-2219-4902>
 Ziyu Huang  <https://orcid.org/0000-0002-8624-1264>
 Rosemary M. Killen  <https://orcid.org/0000-0002-0543-2326>
 Francois Leblanc  <https://orcid.org/0000-0002-5548-3519>
 Amanda Ricketts  <https://orcid.org/0009-0001-6399-6226>
 Daniel W. Savin  <https://orcid.org/0000-0002-1111-6610>

References

- Anderson, B. J., Johnson, C. L., Korth, H., et al. 2011, *Sci*, **333**, 1859
 Anthony, J. W., Bideaux, R. A., Bladh, K. W., & Nichols, M. C. 2001, *Handbook of Mineralogy* (Chantilly, VA: Mineralogical Society of America)
 Behrisch, R., & Eckstein, W. 2007, *Sputtering by Particle Bombardment: Experiments and Computer Calculations from Threshold to MeV Energies*, Vol. 110 (Berlin: Springer)
 Bennett, C. J., Pirim, C., & Orlando, T. M. 2013, *ChRv*, **113**, 9086
 Berendsen, H. J.-C., van Postma, J. P.-M., van Gunsteren, W. F., DiNola, A., & Haak, J. R. 1984, *JChPh*, **81**, 3684
 Biber, H., Brötzner, J., Jäggi, N., et al. 2022, *PSJ*, **3**, 271
 Bringuier, S., Abrams, T., Guterl, J., et al. 2019, *NMEne*, **19**, 1
 Burger, M. H., Killen, R. M., Vervack, R. J., Jr, et al. 2010, *Icar*, **209**, 63
 Cassidy, T. A., & Johnson, R. E. 2005, *Icar*, **176**, 499
 Chaves, L. C., Thompson, M. S., Loeffler, M. J., et al. 2023, *Icar*, **402**, 115634
 Cherniak, D. J. 2010, *RvMG*, **72**, 691
 Christoph, J. M., Minesinger, G. M., Bu, C., Dukes, C. A., & Elkins-Tanton, L. T. 2022, *JGRE*, **127**, e06916
 Deanda, F., & Pearlman, R. S. 2002, *Journal of Molecular Graphics and Modeling*, **20**, 415
 Domingue, D. L., Chapman, C. R., Killen, R. M., et al. 2014, *SSRv*, **181**, 121
 Dong, C., Wang, L., Hakim, A., et al. 2019, *GeoRL*, **46**, 11584
 Dukes, C. A., & Baragiola, R. A. 2015, *Icar*, **255**, 51
 Eckstein, W., & Urbassek, H. M. 2007, in *Sputtering by Particle Bombardment*, ed. R. Behrisch & W. Eckstein (Berlin: Springer), 21
 Ewald, P. P. 1921, *AnP*, **369**, 253
 Fatemi, S., Poppe, A. R., & Barabash, S. 2020, *JGRA*, **125**, e2019JA027706
 Gades, H., & Urbassek, H. M. 1994, *NIMPB*, **88**, 218
 Giletti, B. J., & Shanahan, T. M. 1997, *ChGeo*, **139**, 3
 Glass, A. N., Raines, J. M., Jia, X., et al. 2022, *JGRA*, **127**, e2022JA030969
 Gschneidner, K. A., Jr. 1964, *SSPhy*, **16**, 275
 Hanwell, M. D., Curtis, D. E., Lonie, D. C., et al. 2012, *J. Cheminf.*, **4**, 1
 Hapke, B. 2001, *JGRE*, **106**, 10039
 Heiken, G., Vaniman, D., & French, B. M. 1991, *Lunar Sourcebook: A User's Guide to the Moon* (Cup Archive) (Cambridge: Cambridge Univ. Press)
 Hofsäss, H., Zhang, K., & Mutzke, A. 2014, *ApSS*, **310**, 134
 Huang, Z., Nomura, K., & Wang, J. 2021, *GeoRL*, **48**, e2021GL093509
 Jackson, D. P. 1973, *RadEf*, **18**, 185
 Jackson, D. P. 1975, *CaJPh*, **53**, 1513
 Jäggi, N., Mutzke, A., Biber, H., et al. 2023, *PSJ*, **4**, 86
 Jain, A., Ong, S. P., Hautier, G., et al. 2013, *APLM*, **1**, 11002
 Keller, L. P., & McKay, D. S. 1997, *GeCoA*, **61**, 2331
 Kelly, R. 1986, *NIMPB*, **18**, 388
 Killen, R. M., Morrissey, L. S., Burger, M. H., et al. 2022, *PSJ*, **3**, 139
 Killen, R. M., Sarantos, M., Potter, A. E., & Reiff, P. 2004, *Icar*, **171**, 1
 Lammer, H., Wurz, P., Patel, M. R., et al. 2003, *Icar*, **166**, 238
 Leblanc, F., Schmidt, C., Mangano, V., et al. 2022, *SSRv*, **218**, 2
 Lyngdoh, G. A., Kumar, R., Krishnan, N. M.-A., & Das, S. 2019, *JChPh*, **151**, 64307
 McClintock, W. E., Cassidy, T. A., Merkel, A. W., et al. 2018, *Mercury: The View After MESSENGER* (Cambridge: Cambridge Univ. Press), 371
 McCoy, T. J., Peplowski, P. N., McCubbin, F. M., & Weider, S. Z. 2018, *Mercury: The View after MESSENGER* (Cambridge: Cambridge Univ. Press), 176
 Morrissey, L. S., Pratt, D., Farrell, W. M., et al. 2022a, *Icar*, **379**, 114979
 Morrissey, L. S., Schaible, M. J., Tucker, O. J., et al. 2023, *PSJ*, **4**, 67
 Morrissey, L. S., Tucker, O. J., Killen, R. M., Nakhla, S., & Savin, D. W. 2021, *JAP*, **130**, 13302

- Morrissey, L. S., Tucker, O. J., Killen, R. M., Nakhla, S., & Savin, D. W. 2022b, *ApJL*, **925**, L6
- Mortier, W. J., Ghosh, S. K., & Shankar, S. 1986, *JChS*, **108**, 4315
- Mutzke, A., Schneider, R., Eckstein, W., et al. 2019, SDTrimSP Version 6.00 IPP 2019-02, Max-Planck-Institut für Plasmaphysik doi:10.17617/2.3026474
- Papike, J., Taylor, L., & Simon, S. 1991, Lunar Sourcebook: A User's Guide to the Moon (Cambridge: Cambridge Univ. Press), 121
- Peplowski, P. N., Evans, L. G., Stockstill-Cahill, K. R., et al. 2014, *Icar*, **228**, 86
- Pieters, C. M., & Noble, S. K. 2016, *JGRE*, **121**, 1865
- Pitman, M. C., & Van Duin, A. C.-T. 2012, *JChS*, **134**, 3042
- Plimpton, S. J. 1995, *JCoPh*, **117**, 1
- Poppe, A. R., Farrell, W. M., & Halekas, J. S. 2018, *JGRE*, **123**, 37
- Raines, J. M., Dewey, R. M., Staudacher, N. M., et al. 2022, *JGRA*, **127**, e2022JA030397
- Schaible, M. J., Dukes, C. A., Hutcherson, A. C., et al. 2017, *JGRE*, **122**, 1968
- Schmitz, J., Mutzke, A., Litnovsky, A., et al. 2019, *JNuM*, **526**, 151767
- Sigmund, P. 1969, *PhRv*, **184**, 383
- Sprague, A. L., Emery, J. P., Donaldson, K. L., et al. 2002, *M&PS*, **37**, 1255
- Stukowski, A. 2009, *Model Simul Mat Sci Eng*, **18**, 15012
- Szabo, P. S., Biber, H., Jäggi, N., et al. 2020, *ApJ*, **891**, 100
- Szabo, P. S., Chiba, R., Biber, H., et al. 2018, *Icar*, **314**, 98
- Thompson, A. P., Aktulga, H. M., Berger, R., et al. 2022, *CoPhC*, **271**, 108171
- Thompson, M. W. 1968, *PMag*, **18**, 377
- Tucker, O. J., Farrell, W. M., & Poppe, A. R. 2021, *JGRE*, **126**, e2020JE006552
- Urbassek, H. M. 2007, in Sputtering by Particle Bombardment, ed. R. Behrisch & W. Eckstein (Berlin: Springer), 189
- Van Duin, A. C.-T., Dasgupta, S., Lorant, F., & Goddard, W. A. 2001, *JPCA*, **105**, 9396
- Wolf, D., Keblinski, P., Phillpot, S. R., & Eggebrecht, J. 1999, *JChPh*, **110**, 8254
- Wurz, P., Fatemi, S., Galli, A., et al. 2022, *SSRv*, **218**, 1
- Yang, X., & Hassanein, A. 2014, *ApSS*, **293**, 187
- Yund, R. A. 1983, Feldspar Mineralogy, Vol. 2 (Washington, DC: Mineralogical Society of America), 203
- Zhao, J., Zong, Q., Sun, W., et al. 2024, *JGRA*, **129**, e2023JA032139
- Ziegler, J. F., & Biersack, J. P. 1985, in Treatise on Heavy-ion Science, ed. D. A. Bromley (Boston, MA: Springer), 93